

ViewSplat: View-Adaptive Dynamic Gaussian Splatting for Feed-Forward Synthesis

Moonyeon Jeong¹, Seunggi Min¹, Suhyeon Lee^{2,†}, and Hongje Seong^{1,†}

¹ University of Seoul ² Korea Electronics Technology Institute
{jmy06051,minsk0725,hjseong}@uos.ac.kr suhyeon@keti.re.kr
<https://cvlab-uos.github.io/ViewSplat>

Abstract. We present ViewSplat, a view-adaptive 3D Gaussian splatting network for novel view synthesis from unposed images. While recent feed-forward 3D Gaussian splatting has significantly accelerated 3D scene reconstruction by bypassing per-scene optimization, a fundamental fidelity gap remains. We attribute this bottleneck to the limited capacity of single-step feed-forward networks to regress static Gaussian primitives that satisfy all viewpoints. To address this limitation, we shift the paradigm from static primitive regression to view-adaptive dynamic splatting. Instead of a rigid Gaussian representation, our pipeline learns a view-adaptable latent representation. Specifically, ViewSplat initially predicts base Gaussian primitives alongside the weights of dynamic MLPs. During rendering, these MLPs take target view coordinates as input and predict view-dependent residual updates for each Gaussian attribute (*i.e.*, 3D position, scale, rotation, opacity, and color). This mechanism, which we term view-adaptive dynamic splatting, allows each primitive to rectify initial estimation errors, effectively capturing high-fidelity appearances. Extensive experiments demonstrate that ViewSplat achieves state-of-the-art fidelity while maintaining fast inference (17 FPS) and real-time rendering (154 FPS).

Keywords: Novel View Synthesis · 3D Gaussian Splatting · Pose-Free Reconstruction

1 Introduction

3D Gaussian Splatting (3DGS) [17] has recently emerged as a powerful representation in 3D computer vision, enabling high-fidelity real-time rendering. While traditional 3DGS frameworks rely on per-scene optimization, recent efforts have focused on generalizable feed-forward architectures [3, 5, 30, 36, 39]. These models predict scene representations directly from a few input images, enabling instant 3D reconstruction of unseen scenes and high-quality novel view synthesis (NVS) without costly target scene optimization.

A major bottleneck in these generalizable pipelines is the heavy reliance on accurate camera poses, typically pre-computed via Structure-from-Motion

[†]Co-corresponding authors.

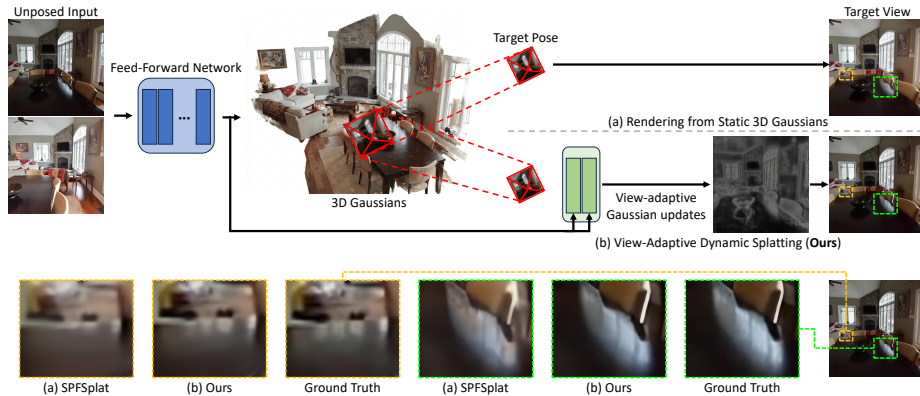


Fig. 1: Given unposed images as input, the feed-forward network reconstructs 3D Gaussians. While (a) rendering from static 3D Gaussians often suffers from blurred details, (b) our method introduces view-adaptive Gaussian updates conditioned on the target pose to refine the Gaussians dynamically. As shown in the bottom panels, our approach improves the reconstruction of fine-grained details (e.g., sharp edges and specular reflections) compared to SPFSplat [11].

(SfM) [27]. To address this, recent works [11, 12, 16, 28] leverage 3D foundation models—such as DUST3R [33], MAST3R [18], and VGGT [32]—to facilitate pose-free reconstruction. These frameworks enable the joint estimation of camera parameters and 3D Gaussian primitives [11, 14], delivering robust 3D reconstructions directly from uncalibrated, in-the-wild images.

Despite these advancements, a significant fidelity gap remains between feed-forward approaches and optimization-based methods [15, 21, 23, 37, 43]. We attribute this bottleneck to the limited capacity of feed-forward networks to regress static Gaussian primitives that satisfy all potential viewpoints. These models typically employ a single-step regression to predict all Gaussian attributes (*i.e.*, 3D position, scale, rotation, opacity, and spherical harmonics (SH) coefficients). However, regressing optimal representations is an ill-posed task for a single forward pass, especially when dealing with complex geometries or non-Lambertian surfaces. While optimization-based methods can refine these attributes over thousands of iterations to capture sharp specularities and view-dependent SH coefficients, feed-forward models lack the capacity to *rectify* their initial predictions during inference.

To address this limitation, we propose ViewSplat, a novel framework that shifts the paradigm from static primitive regression to view-adaptive dynamic splatting (Fig. 1). The key insight behind ViewSplat is that achieving high-fidelity 2D rendering from a *specific* view is relatively straightforward, provided the underlying 3D primitives can be tailored to that viewpoint. We leverage this observation by shifting the network’s objective: instead of struggling to predict universal 3D Gaussians, the network focuses on generating view-specific updates that are far more feasible to learn. This shift allows our model to rectify initial errors and capture complex view-dependent details that a static model would

otherwise miss. Building upon a pose-free feed-forward architecture [11, 12], our model introduces a mechanism that dynamically updates Gaussian primitives for every target viewpoint on-the-fly.

Specifically, ViewSplat predicts two components for a given scene: a set of base Gaussian primitives and the weights of dynamic MLPs. Unlike standard MLPs with fixed parameters, these dynamic MLPs are conditioned on the input scene context. During the rendering stage, these MLPs take the target view coordinates as input and predict view-dependent residual updates for all Gaussian attributes, including 3D position, scale, rotation, opacity, and SH coefficients. This allows each primitive to undergo geometric and photometric refinement tailored to the specific viewpoint. Consequently, ViewSplat can effectively compensate for initial estimation errors and synthesize high-frequency, non-Lambertian effects that are typically lost in static feed-forward representations.

Our approach maintains the efficiency required for practical applications, achieving fast inference (17 FPS) and high-speed rendering (154 FPS) while significantly outperforming existing generalizable models. Our main contributions are summarized as follows:

- We identify the static primitive bottleneck in feed-forward 3DGS and propose view-adaptive representations for high-fidelity synthesis.
- We introduce ViewSplat, which utilizes scene-conditioned dynamic MLPs to predict view-dependent residuals for all Gaussian attributes, enabling the model to rectify geometric and appearance errors on-the-fly.
- We demonstrate that ViewSplat achieves state-of-the-art performance on standard benchmark sets, effectively capturing complex view-dependent effects without the need for costly per-scene optimization or pre-computed poses.

2 Related Work

2.1 Feed-Forward 3D Gaussian Splatting

The landscape of 3DGS [17] has recently diversified, with significant research efforts increasingly directed toward feed-forward generalizable architectures that enable instant 3D reconstruction and NVS. Early generalizable 3DGS methods are pose-required, relying on accurate camera parameters to aggregate multi-view features or construct cost volumes. For instance, pixelSplat [3] and MVSplat [5] leverage epipolar transformers for depth estimation and Gaussian primitive prediction. Similarly, large-scale models such as LGM [30], GRM [36], and GS-LRM [39] encode camera poses via Plücker ray embeddings. While effective, such methods rely on pre-computed poses through SfM [27], which is computationally expensive and often unreliable in sparse-view scenarios.

To overcome these constraints, pose-free feed-forward methods have emerged. Supervised pose-free models like Splatt3R [28] and NoPoSplat [38] predict 3D Gaussians in a canonical space without inference-time poses, yet they still require

ground-truth poses for training supervision. More recently, self-supervised approaches such as SelfSplat [16], PF3plat [9], SPFSplat [11], and SPFSplatV2 [12] have effectively eliminated this dependency. In particular, SPFSplat and SPFSplatV2 leverage the large-scale 3D foundation model backbone such as MAST3R [18] and VGGT [32] to jointly estimate camera poses and 3D geometry in a unified end-to-end pipeline.

Despite these advancements, existing feed-forward 3DGS models are fundamentally constrained by static primitive regression. By predicting a fixed set of Gaussian attributes in a single pass, these methods struggle to reconcile conflicting visual information across diverse viewpoints, leading to blurred details and a failure to capture non-Lambertian effects like sharp specularities. Our ViewSplat breaks this bottleneck by shifting from rigid regression to view-adaptive refinement. Built upon the self-supervised, pose-free feed-forward frameworks [11, 12], we introduce a dynamic update mechanism that *rectifies* Gaussian parameters on-the-fly for each target viewpoint, enabling high-fidelity synthesis that was previously only attainable through per-scene optimization.

2.2 View-Dependent 3D Representation

Modeling view-dependent effects is a long-standing challenge in neural rendering. In Neural Radiance Fields (NeRF) [25], the standard approach involves conditioning the radiance MLP on the viewing direction to capture view-dependent color. However, this often struggles to represent complex surface properties, particularly non-Lambertian and sharp specular effects. To address this limitation, several works [1, 2, 29, 41] decompose visual appearance into intrinsic properties—such as lighting and materials—typically parameterized via Bidirectional Reflectance Distribution Functions (BRDFs). Ref-NeRF [31] further enhances specular fidelity by utilizing reflection vectors. While effective, these implicit methods often require auxiliary geometric priors, such as those derived from signed distance functions (SDF) [19, 22], to obtain high-quality normals for accurate shading.

The introduction of 3DGS [17] has opened new avenues for explicit view-dependent modeling. While 3DGS originally employs low-order SH to represent view-dependent color, SH coefficients frequently lack the frequency bandwidth necessary to capture sharp specularities. To overcome this limitation, recent extensions like GaussianShader [15] and RTR-GS [43] integrate explicit shading models into the Gaussian framework. Other approaches, such as Spec-Gaussian [37], introduce anisotropic spherical Gaussians to provide more flexible parameterization than traditional SH. MirrorGaussian [21] tackles the specific challenge of mirror reflections by incorporating symmetry-based Gaussian reflections. Beyond appearance, Scaffold-GS [23] explores structural stabilization of Gaussian attributes across viewpoints using an anchor-based representation.

While these advancements have significantly improved the fidelity of view-dependent rendering, they remain predominantly tied to per-scene optimization. This dependency results in high computational costs and a lack of generalization to unseen scenes. In contrast, ViewSplat addresses view dependency within a feed-forward framework. Note that our use of *dynamic* refers to viewpoint-conditioned

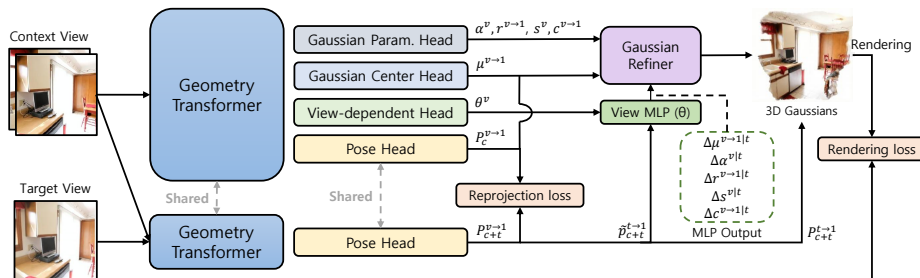


Fig. 2: Architecture of ViewSplat. Built upon a shared geometry transformer backbone [18, 32], our framework simultaneously predicts canonical 3D Gaussians and camera poses from unposed images using Gaussian heads and a pose head. To accurately capture view-dependent effects, a view-dependent head dynamically generates per-pixel view MLPs, which takes the target pose as input to predict residual offsets for Gaussians. These offsets are then applied to refine the canonical Gaussians during rendering.

attribute modulation rather than temporal deformation as seen in 4D dynamic scene rendering [24, 35]. This allows for efficient, high-fidelity reconstruction and synthesis of complex view-dependent effects without the need for scene-specific training or costly iterative optimization.

3 Method

We propose ViewSplat, a view-dependent feed-forward 3D Gaussian splatting framework that jointly reconstructs 3D Gaussians and estimates camera poses directly from multi-view images without requiring ground-truth poses. Given a set of images, the network predicts the 3D Gaussian parameters in a canonical space defined by the first input image, which serves as the global reference coordinate frame. Simultaneously, it estimates the camera pose for each view, representing the canonical-to-camera transformation. Leveraging this relative pose information, our model predicts view-dependent residual offsets for the Gaussian parameters. These offsets are added to the canonical Gaussians to refine their attributes, enabling rendering of view-dependent effects such as specular highlights.

An overview of our architecture is illustrated in Fig. 2. We first present the preliminaries of our pose-free Gaussian reconstruction framework based on SPFSplat [11, 12] in Sec. 3.1. We then introduce our proposed view-dependent head in Sec. 3.2 and detail the view-dependent Gaussian refinement process in Sec. 3.3. Finally, we describe the training objective, including the rendering and reprojection losses, in Sec. 3.4.

3.1 Preliminaries

Our framework builds upon prior pose-free Gaussian reconstruction architectures, including SPFSplat and its subsequent variants [11, 12]. These models adopt a geometry transformer backbone—such as MAST3R [18] and VGGT [32]—along

with pose and Gaussian prediction heads to reconstruct a 3D scene from N unposed images $\{I^v\}_{v=1}^N$.

Geometry Transformer. A ViT-based [6] encoder-decoder architecture is employed to extract multi-view feature tokens. The ViT encoder processes patchified RGB inputs through self-attention, after which the decoder enables cross-view interaction to aggregate geometric and appearance information across the N encoded views.

The specific interaction mechanism is determined by the backbone. MAST3R-based models employ pairwise cross-attention between views, whereas the VGGT-based V2-L variant performs global self-attention over a unified token sequence. In SPFSplatV2 and V2-L, a masked attention strategy is additionally introduced in the decoder to improve camera pose estimation and geometry reconstruction. The resulting tokens, enriched with global 3D context, serve as the foundation for both the baseline Gaussian reconstruction and our proposed view-dependent refinement.

Canonical 3D Gaussian Reconstruction. To reconstruct the 3D scene, two Dense Prediction Transformer (DPT)-based heads [26] predict 3D Gaussian parameters in a dense, per-pixel manner. The first DPT head, referred to as Gaussian center head, processes the decoded tokens to predict per-pixel 3D coordinates that define the Gaussian centers. The second head, referred to as Gaussian parameter head, estimates the remaining Gaussian attributes for each pixel. These 3D Gaussians are aligned in a canonical space, where the first input view I_1 serves as the global reference coordinate frame. Specifically, the predicted Gaussians are parameterized as:

$$\{\mathcal{G}^{v \rightarrow 1}\}_{v=1, \dots, N} = \{(\mu_j^{v \rightarrow 1}, \alpha_j^v, r_j^{v \rightarrow 1}, s_j^v, c_j^{v \rightarrow 1})\}_{j=1, \dots, H \times W}, \quad (1)$$

where each Gaussian primitive consists of a center position $\mu \in \mathbb{R}^3$, a rotation quaternion $r \in \mathbb{R}^4$, a scale vector $s \in \mathbb{R}^3$, an opacity value $\alpha \in \mathbb{R}$, and SH coefficients c . Following DPT, high-resolution skip connections are incorporated to preserve fine-grained spatial details from the input images.

Pose Estimation. For pose-free rendering, the pose head estimates the camera poses in a single feed-forward step. By taking the concatenated and pooled representations from the encoder and decoder, a lightweight MLP outputs a 10-dimensional relative pose comprising a 6D rotation representation and a 4D homogeneous translation vector $[t_x, t_y, t_z, 1]^\top$, following [4]. This pose is then converted into a homogeneous transformation matrix $P^{v \rightarrow 1} \in \mathbb{R}^{4 \times 4}$ which is defined as:

$$P^{v \rightarrow 1} = \begin{bmatrix} R^{v \rightarrow 1} & t^{v \rightarrow 1} \\ \mathbf{0}^\top & 1 \end{bmatrix}, \quad (2)$$

where $R^{v \rightarrow 1} \in \mathbb{R}^{3 \times 3}$ is the rotation matrix and $t^{v \rightarrow 1} \in \mathbb{R}^3$ is the translation vector. This matrix is the relative transformation of any input view I_v to the

canonical reference view I_1 . To establish a consistent global coordinate system, the first input view I_1 is defined as the origin, explicitly assigning its canonical pose as:

$$P^{1 \rightarrow 1} = \begin{bmatrix} I & \mathbf{0} \\ \mathbf{0}^\top & 1 \end{bmatrix}, \quad (3)$$

where I represents the identity matrix and $\mathbf{0}$ denotes the zero translation vector.

During training, to synthesize novel views without ground-truth poses, the model additionally predicts the poses of target views, denoted as $P^{t \rightarrow 1}$. As illustrated in Fig. 2, this target pose estimation leverages features from both context and target views to better capture the global scene structure. Importantly, to prevent information leakage, the initial Gaussian reconstruction is strictly conditioned on the context views, and remains independent of the target pose prediction.

3.2 View-Dependent Head

As described in Sec. 3.1, the baseline pipeline reconstructs a static set of Gaussians in the canonical space. However, due to its fixed geometry and the inherent limitations of SH, this static formulation often struggles to capture complex view-dependent effects, such as specular highlights, reflections, and subtle appearance variations. To address this limitation, we introduce a DPT-based view-dependent head that adopts a hypernetwork architecture [8] to predict per-pixel residual offsets for the Gaussian parameters. Instead of directly outputting offsets, this head takes feature tokens from the geometry transformer to capture rich geometric and material context, and dynamically generates pixel-wise parameters for a secondary network, which we refer to as view MLP.

This design allows the model to generate pixel-specific response functions tailored to the local properties of the scene. The generated view MLPs are conditioned on the target camera pose and compute the corresponding Gaussian parameter offsets. By predicting these view MLPs on the fly, the architecture can flexibly adapt its refinement strategy to the specific requirements of the target viewpoint. For instance, the head can generate a more complex mapping for specular surfaces to capture shifting reflections, while maintaining simpler functions for diffuse regions. This separation between context-driven weight generation and pose-driven offset calculation enables the model to capture intricate, high-frequency appearance variations without being constrained by a static, predefined parameter space.

3.3 View-Dependent Gaussian Refinement

We now describe how the generated view MLPs utilize the target pose and refine the canonical Gaussians. The view MLP takes a 4D per-pixel target pose representation as input to compute Gaussian parameter offsets. This 4D pose representation, comprising a 3D unit viewing direction and a 1D distance term, is carefully derived from the target camera extrinsics $P^{t \rightarrow 1}$.

Target Pose Reparameterization. The raw target extrinsic $P^{t \rightarrow 1} \in \mathbb{R}^{4 \times 4}$ is a homogeneous world-to-camera transformation matrix composed of a 3×3 rotation matrix and a 3D translation vector, as defined in Eq. (2). Directly feeding this full transformation matrix into the network is undesirable as the complex mathematical constraints inherent in transformation matrices (*e.g.*, rotation orthogonality) are difficult for an MLP to optimize. To alleviate this, we reparameterize the target pose into a compact and geometrically meaningful representation consisting of a 3D unit viewing direction and a 1D distance. This design reduces the input dimensionality from 16 scalar elements to 4, while retaining essential view-dependent cues, facilitating network learning.

Gaussian Refinement. Given the 4D target pose representation, the view MLP predicts parameter offsets for the Gaussians at each pixel. Specifically, the network outputs the following offset values:

$$\{\Delta \mathcal{G}^{v \rightarrow 1}\}_{v=1, \dots, N} = \{(\Delta \mu_j^{v \rightarrow 1|t}, \Delta \alpha_j^{v|t}, \Delta r_j^{v \rightarrow 1|t}, \Delta s_j^{v|t}, \Delta c_j^{v \rightarrow 1|t})\}_{j=1, \dots, H \times W}. \quad (4)$$

These offsets encode how each Gaussian, originating from a specific context view and pixel, should adapt when observed from the target viewpoint t . The predicted offsets are directly applied to the canonical 3D Gaussians defined in Eq. (1) via element-wise residual addition (*e.g.*, $\hat{\mu} = \mu + \Delta \mu$), yielding the final refined parameters $\{\hat{\mathcal{G}}^{v \rightarrow 1}\}_{v=1, \dots, N}$. The rasterizer then renders the novel view from the target pose $P^{t \rightarrow 1}$:

$$\hat{I}^t = \mathcal{R}(P^{t \rightarrow 1}, \{\hat{\mathcal{G}}^{v \rightarrow 1}\}_{v=1, \dots, N}). \quad (5)$$

3.4 Loss Function

Following the training strategy of SPFSplat [11], our model is optimized end-to-end without relying on ground-truth camera poses. The overall training objective consists of an image rendering loss \mathcal{L}_{render} and a geometric reprojection loss \mathcal{L}_{reproj} . Specifically, \mathcal{L}_{render} is formulated as a weighted combination of MSE photometric loss and LPIPS [40] perceptual loss to balance low-level photometric accuracy and high-level perceptual similarity. To stabilize training in the canonical space and enforce explicit geometric constraints, we employ \mathcal{L}_{reproj} , which penalizes the distance between 2D pixel coordinates and the projected 3D Gaussian centers using estimated relative poses. The total loss is defined as:

$$\mathcal{L}_{total} = \mathcal{L}_{render} + \lambda_{reproj} \mathcal{L}_{reproj}, \quad (6)$$

where λ_{reproj} is a weighting factor. We provide full mathematical derivations and detailed hyperparameter settings for each loss term in the appendix.

4 Experiments

We evaluate the performance of our method on novel view synthesis and cross-dataset generalization across multiple datasets. In addition, we conduct comprehensive ablation studies to analyze the contribution of each component.

4.1 Experimental Settings

Datasets. We train and evaluate our method on the RealEstate10K (RE10K) [42], which contains large-scale real estate videos, and ACID [20], which consists of nature scenes captured by aerial drones. The camera poses for both datasets are obtained via SfM, but our method operates in a strictly pose-free manner, entirely bypassing the need for such pre-computed information. We adopt the official train–test splits used in prior works [3, 5, 11, 38]. To rigorously assess performance, we follow the evaluation protocol of [11, 38], which evaluates our method under varying levels of camera overlap. We categorize input pairs into three groups based on image overlap ratios—small (0.05%–0.3%), medium (0.3%–0.55%), and large (0.55%–0.8%)—determined using a pre-trained dense image matching method [7]. Furthermore, to validate cross-dataset generalization, we follow [5, 11, 38] and evaluate our model on the object-centric DTU dataset [13].

Baselines. We compare our method with several baselines for novel view synthesis. These baselines include pose-required models (pixelSplat [3] and MVSSplat [5]), supervised pose-free models (CoPoNerf [10], Splatt3R [28], and NoPoSplat [38]), and self-supervised models (SelfSplat [16], PF3plat [9], SPFSplat [11], and SPFSplatV2 [12]).

Evaluation Protocols. We assess the quality of novel view synthesis using standard metrics: pixel-level PSNR, patch-level SSIM [34], and feature-level LPIPS [40].

During NVS evaluation, target views are conventionally rendered using ground-truth poses [3, 5, 10, 28]. Alternative approaches include rendering with estimated target poses (*e.g.*, PF3plat [9], SelfSplat [16], SPFSplat [11], and SPFSplatV2 [12]) or employing an evaluation-time pose alignment (EPA) strategy (NoPoSplat [38]), which optimizes the target poses during evaluation while freezing the reconstructed Gaussians. In our experiments, we evaluate our method using the estimated target poses. This setting allows us to jointly evaluate the reconstruction quality and the alignment between the estimated poses and the learned Gaussians.

4.2 Implementation Details

We implement ViewSplat in PyTorch, utilizing a CUDA-based 3DGS renderer with gradient support for camera poses. All models are trained on multiple NVIDIA RTX 4090 GPUs, while inference is performed on a single GPU.

Following prior works [11, 12], we adopt the geometry transformer backbones from MAST3R [18] for the SPFSplat and SPFSplatV2 architectures, and VGGT [32] for V2-L variant. To ensure stable convergence, we initialize the geometry transformer, Gaussian parameter head, Gaussian center head, and pose head using pre-trained weights from the corresponding SPFSplat, SPFSplatV2, or V2-L models. The remaining component, our view-dependent head, is zero-initialized; this allows the network to initially preserve the baseline static reconstruction while progressively learning to incorporate view-adaptive refinements.

The view-dependent head generates pixel-wise view MLPs with a single hidden layer of 16 dimensions. All experiments are conducted at a resolution of 256×256 ,

except for the V2-L variant, which follows its backbone’s default resolution of 224×224 .

Training Strategy. We adopt a frozen-backbone training strategy, where the pre-trained weights of the base models (SPFSplat or SPFSplatV2) remain fixed while only the view-dependent head is optimized. We use the Adam optimizer with a learning rate of 1×10^{-4} and a batch size of 12. Each batch contains a single scene with its corresponding input and target views. Consistent with prior work, the frame distance between input views is progressively increased during training to facilitate curriculum learning.

Table 1: Performance comparison of novel view synthesis on the RE10K dataset [42]. Results using the **ViewSplat** framework are highlighted in **bold**, demonstrating consistent performance gains across all SPFSplat variants. * indicates the use of evaluation-time pose alignment (EPA) strategy.

Method	Small			Medium			Large			Average		
	PSNR \uparrow	SSIM \uparrow	LPIPS \downarrow	PSNR \uparrow	SSIM \uparrow	LPIPS \downarrow	PSNR \uparrow	SSIM \uparrow	LPIPS \downarrow	PSNR \uparrow	SSIM \uparrow	LPIPS \downarrow
<i>Pose-Required</i>												
pixelSplat	20.277	0.719	0.265	23.726	0.811	0.180	27.152	0.880	0.121	23.859	0.808	0.184
MVSplat	20.371	0.725	0.250	23.808	0.814	0.172	27.466	0.885	0.115	24.012	0.812	0.175
<i>Supervised Pose-Free</i>												
CoPoNeRF	17.393	0.585	0.462	18.813	0.616	0.392	20.464	0.652	0.318	18.938	0.619	0.388
Splatt3R	17.789	0.582	0.375	18.828	0.607	0.330	19.243	0.593	0.317	18.688	0.337	0.596
NoPoSplat*	22.514	0.784	0.210	24.899	0.839	0.160	27.411	0.883	0.119	25.033	0.838	0.160
<i>Self-Supervised Pose-Free</i>												
SelfSplat	14.828	0.543	0.469	18.857	0.679	0.328	23.338	0.798	0.208	19.152	0.680	0.328
PF3plat	18.358	0.668	0.298	20.953	0.741	0.231	23.491	0.795	0.179	21.042	0.739	0.233
SPFSplat	22.897	0.792	0.201	25.334	0.847	0.153	27.947	0.894	0.110	25.484	0.847	0.153
+ViewSplat	23.562	0.802	0.191	26.193	0.858	0.143	28.886	0.904	0.104	26.317	0.857	0.144
SPFSplatV2	23.123	0.800	0.195	25.542	0.853	0.149	28.143	0.897	0.110	25.693	0.853	0.149
+ViewSplat	23.761	0.808	0.185	26.353	0.862	0.139	28.978	0.906	0.102	26.468	0.861	0.140
SPFSplatV2-L	23.138	0.804	0.184	25.518	0.856	0.136	28.081	0.899	0.099	25.668	0.855	0.137
+ViewSplat	24.129	0.819	0.168	26.686	0.871	0.123	29.274	0.912	0.088	26.798	0.870	0.124

Table 2: Performance comparison of novel view synthesis on the ACID dataset [20].

Method	Small			Medium			Large			Average		
	PSNR \uparrow	SSIM \uparrow	LPIPS \downarrow	PSNR \uparrow	SSIM \uparrow	LPIPS \downarrow	PSNR \uparrow	SSIM \uparrow	LPIPS \downarrow	PSNR \uparrow	SSIM \uparrow	LPIPS \downarrow
<i>Pose-Required</i>												
pixelSplat	22.088	0.655	0.284	25.525	0.777	0.197	28.527	0.854	0.139	25.889	0.780	0.194
MVSplat	21.412	0.640	0.290	25.150	0.772	0.198	28.457	0.854	0.137	25.561	0.775	0.195
<i>Supervised Pose-Free</i>												
CoPoNeRF	18.651	0.551	0.485	20.654	0.595	0.418	22.654	0.652	0.343	20.950	0.606	0.406
Splatt3R	17.419	0.501	0.434	18.257	0.514	0.405	18.134	0.508	0.395	18.060	0.510	0.407
NoPoSplat*	23.087	0.685	0.258	25.624	0.777	0.193	28.043	0.841	0.144	25.961	0.781	0.189
<i>Self-Supervised Pose-Free</i>												
SelfSplat	18.301	0.568	0.408	21.375	0.676	0.314	25.219	0.792	0.214	22.089	0.694	0.298
PF3plat	18.112	0.537	0.376	20.732	0.615	0.307	23.607	0.710	0.228	21.206	0.632	0.293
SPFSplat	22.667	0.665	0.262	25.620	0.773	0.192	28.607	0.856	0.136	26.070	0.781	0.186
+ViewSplat	23.035	0.671	0.255	26.161	0.782	0.184	29.395	0.869	0.124	26.661	0.790	0.177
SPFSplatV2	22.944	0.679	0.255	25.849	0.784	0.187	28.766	0.862	0.133	26.284	0.791	0.182
+ViewSplat	23.264	0.685	0.249	26.398	0.794	0.179	29.561	0.875	0.122	26.873	0.801	0.173
SPFSplatV2-L	23.640	0.706	0.225	26.272	0.801	0.166	28.938	0.868	0.120	26.674	0.806	0.162
+ViewSplat	24.234	0.718	0.214	27.090	0.815	0.154	29.931	0.885	0.106	27.509	0.820	0.149

4.3 Results

Novel View Synthesis. We evaluate ViewSplat on the RE10K and ACID benchmarks, and the quantitative results are summarized in Tab. 1 and Tab. 2.

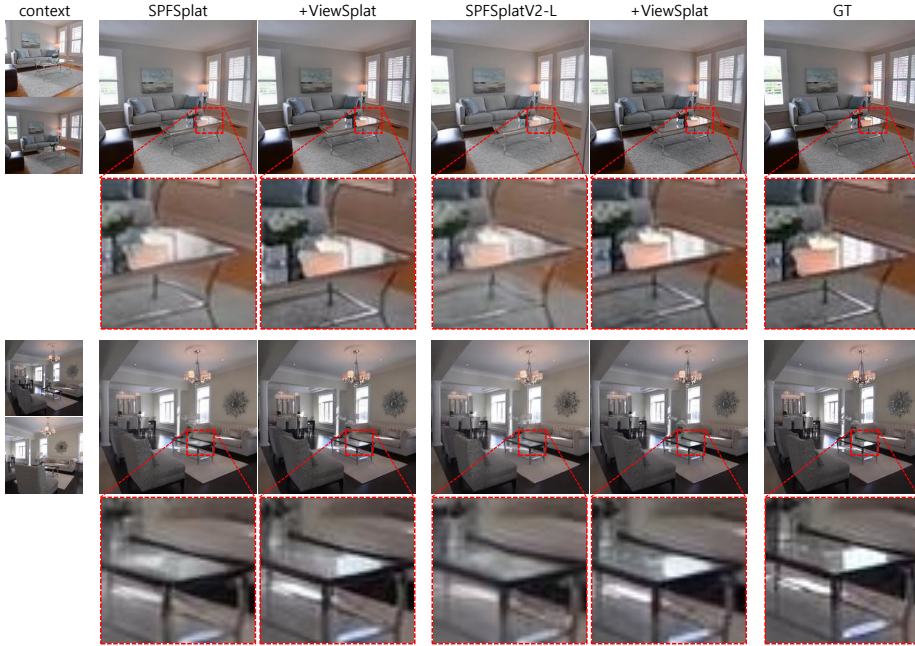


Fig. 3: Qualitative comparison on RE10K. Compared to baseline methods, our approach accurately reconstructs sharp reflections.

Our framework, particularly the V2-L variant, consistently achieves new state-of-the-art performance across all metrics. A key finding is the orthogonal performance gain provided by our view-adaptive refinement. Across all backbone variants—SPFSplat, V2, and V2-L—ViewSplat consistently yields substantial improvements in rendering fidelity. This consistency underscores the scalability and robustness of our approach in capturing intricate view-dependent details across diverse environments, from structured interiors to complex natural landscapes. Qualitative comparisons in Fig. 3 further demonstrate ViewSplat’s ability to synthesize high-frequency specularities and maintain geometric consistency, resulting in photorealistic novel views. Additional qualitative results are provided in the appendix.

Table 3: Comparison of efficiency on a single NVIDIA RTX 4090 GPU on the RE10K.

Method	Params↓ (B)	Inference time↓ (s)	Rendering Speed↑ (FPS)
SPFSplat	0.616	0.046	386
+ViewSplat	0.658	0.057	154
SPFSplatV2	0.613	0.039	390
+ViewSplat	0.655	0.052	149
SPFSplatV2-L	1.223	0.066	231
+ViewSplat	1.256	0.068	90

Table 4: Comparison of rendering performance between baseline SPFSplat [11] with varying SH degrees and proposed ViewSplat on the RE10K. The **best** results are highlighted.

Method	SH Degree	PSNR↑	SSIM↑	LPIPS↓
SPFSplat (Std.)	4	25.486	0.847	0.153
SPFSplat	6	25.408	0.845	0.154
SPFSplat	8	25.418	0.845	0.153
+ViewSplat	4	26.317	0.857	0.144

Efficiency. We evaluate the computational efficiency of our framework on a single NVIDIA RTX 4090 GPU, as summarized in Tab. 3. The integration of the ViewSplat module introduces only marginal overhead in inference time (*i.e.*, the network’s forward pass), which encompasses both the reconstruction of 3D Gaussians from input pairs and the generation of pixel-wise view MLP parameters. Although the rendering speed (FPS) decreases due to the dynamic refinement of 3D Gaussian attributes conditioned on the target view pose, the models consistently maintain real-time performance (≥ 30 FPS). These results demonstrate that ViewSplat effectively balances improved rendering quality with the practical requirement of real-time rendering, ensuring its suitability for interactive applications.

Analysis of View-Dependent Modeling. To further validate the effectiveness of our view-dependent refinement framework, we compare ViewSplat against the baseline SPFSplat with varying SH degrees (Tab. 4). While increasing the SH degree of the baseline model from 4 to 8 yields negligible improvement and may even slightly degrade performance, ViewSplat with SH degree 4 significantly outperforms all baseline variants. This suggests that standard SH-based representations reach a performance limit in pose-free settings, whereas our view-dependent refinement provides superior expressive capacity for capturing complex specularities and non-linear appearances.

Table 5: Cross-dataset generalization. All methods are trained on RE10K and evaluated in a zero-shot setting on ACID and DTU. Results using the **ViewSplat** framework are highlighted in **bold**, demonstrating consistent performance gains across all SPFSplat variants.

Method	ACID			DTU		
	PSNR \uparrow	SSIM \uparrow	LPIPS \downarrow	PSNR \uparrow	SSIM \uparrow	LPIPS \downarrow
<i>Pose-Required</i>						
pixelSplat	25.477	0.770	0.207	15.067	0.539	0.341
MVSplat	25.525	0.773	0.199	14.542	0.537	0.324
<i>Supervised Pose-Free</i>						
NoPoSplat*	25.764	0.776	0.199	17.899	0.629	0.279
<i>Self-Supervised Pose-Free</i>						
SelfSplat	22.204	0.686	0.316	13.249	0.434	0.441
PF3splat	20.726	0.610	0.308	12.972	0.407	0.464
SPFSplat	25.965	0.781	0.190	16.550	0.579	0.270
+ViewSplat	26.595	0.793	0.179	16.864	0.589	0.259
SPFSplatV2	26.220	0.789	0.185	16.793	0.584	0.265
+ViewSplat	26.761	0.798	0.175	17.034	0.588	0.258
SPFSplatV2-L	26.361	0.796	0.169	17.739	0.653	0.228
+ViewSplat	27.169	0.810	0.154	18.174	0.665	0.215

Cross-Dataset Generalization. To evaluate the generalization capability of our method, we conduct zero-shot evaluations on the ACID and DTU datasets after training exclusively on RE10K. The results in Tab. 5 and Fig. 4 demonstrate that our ViewSplat framework, particularly when integrated with the SPFSplatV2-L backbone, consistently outperforms all baselines, including pose-required and supervised pose-free methods. Notably, we observe consistent performance gains

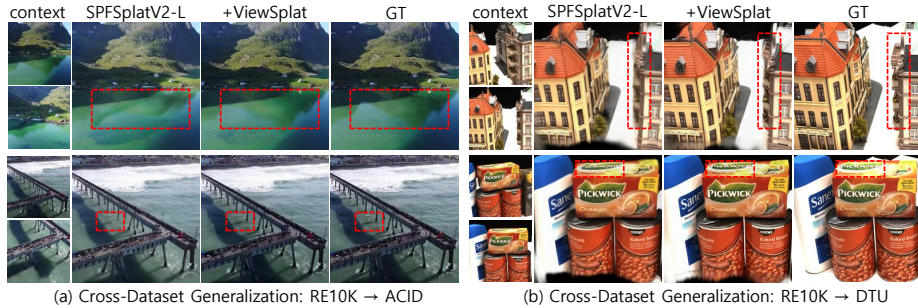


Fig. 4: Qualitative results of cross-dataset generalization.

across all backbone variants (SPFSplat, V2, and V2-L) when our view-dependent refinement is incorporated. This stable improvement suggests that our module learns transferable view-dependent representations that generalize effectively to out-of-distribution environments, ranging from the natural landscape of ACID to the object-centric scenes of DTU.

Table 6: Effectiveness of refinement components. We evaluate the contribution of residual offsets for each Gaussian parameter on RE10K. $\Delta\mu$, $\Delta\alpha$, Δr , Δs , and Δc denote the residual offsets for mean, opacity, rotation, scale, and SH coefficients, respectively. The **best** and second-best results are highlighted.

Method	$\Delta\mu$	$\Delta\alpha$	$\Delta(r, s, c)$	PSNR \uparrow	SSIM \uparrow	LPIPS \downarrow
(1) Baseline (SPFSplat)	×	×	×	25.484	0.847	0.153
(2) $\Delta(\mu, \alpha)$ only	✓	✓	×	25.760	0.850	0.155
(3) $\Delta(r, s, c)$ only	×	×	✓	26.241	<u>0.856</u>	0.146
(4) w/o $\Delta\alpha$	✓	×	✓	15.684	0.555	0.525
(5) w/o $\Delta\mu$	×	✓	✓	<u>26.307</u>	0.857	<u>0.145</u>
(6) Full (ViewSplat)	✓	✓	✓	26.317	0.857	0.144



Fig. 5: Artifacts from decoupled μ/α refinement.

4.4 Ablation Studies

Ablation on Refinement Components. Tab. 6 shows that most refinement subsets improve performance over the baseline. However, case (4) suffers catastrophic degradation when mean offsets are applied without corresponding opacity refinement. This decoupling leads to severe artifacts, blurring, and structural collapse, as shown in Fig. 5. These results confirm that spatial shifts must be synchronized with visibility updates to preserve structural coherence. By jointly optimizing all parameters, our full model (6) achieves the best performance across all metrics, underscoring the importance of holistic refinement.

Ablation on Training Strategies. Tab. 7 compares the impact of different initialization and freezing strategies. Our main ViewSplat model, which trains only the view-dependent head while freezing the backbone initialized with SPFSplat weights, achieves superior performance compared to training all parameters from MAST3R weights. For the MAST3R-initialized variant, we adopt learning rates of 1×10^{-5} for the encoder and decoder, and 1×10^{-4} for the heads. The best performance is achieved by unfreezing the backbone and fine-tuning the entire model (ViewSplat w/ FT), with all learning rates reduced by a factor of 10.

Table 7: Comparison of different training strategies on RE10K. We compare our proposed ViewSplat (SPFSplat-initialized with frozen backbone) against two variants: (1) a fully fine-tuned version starting from our main ViewSplat model, and (2) a model trained from MAST3R pre-trained weights without freezing. The **best** results are highlighted.

Strategy	Pre-trained Weight	Freeze Pre-trained	PSNR \uparrow	SSIM \uparrow	LPIPS \downarrow
ViewSplat (MASt3R-init)	MASt3R	×	26.192	0.854	0.140
ViewSplat	SPFSplat	✓	26.317	0.857	0.144
ViewSplat (w/ FT)	ViewSplat	×	26.459	0.859	0.141

However, jointly training the backbone causes significant additional computational overhead; given that the performance gains are relatively marginal compared to the increased training cost, we adopt the frozen backbone configuration as our default setting. These results indicate that SPFSplat-based initialization provides a robust starting point, while global fine-tuning can further enhance performance at the cost of higher resource requirements. More ablation studies are included in the supplementary material.

4.5 Limitations

Despite the improvements achieved by ViewSplat through its view-dependent refinement framework, it inherits a key limitation of the baseline SPFSplat: the inability to synthesize content in unobserved regions. Since both methods are reconstruction-based and lack generative priors, they cannot hallucinate missing information, which results in blurry artifacts or empty regions in sparse-view areas, as illustrated in Fig. 6. This limitation highlights the inherent challenge of achieving complete scene recovery without incorporating generative modeling.



Fig. 6: Limitations: visual artifacts in unobserved regions.

5 Conclusion

We present ViewSplat, a view-adaptive framework that addresses the fidelity bottleneck in feed-forward 3D Gaussian splatting. By shifting from static primitive regression to view-adaptive dynamic splatting, our method refines Gaussian attributes conditioned on the target view, enabling the modeling of complex view-dependent appearances that rigid representations often fail to model. ViewSplat achieves state-of-the-art fidelity while maintaining real-time rendering (154 FPS) across multiple benchmarks, without requiring pre-computed poses. We hope our view-adaptive paradigm inspires future research into more flexible and high-fidelity 3D representations for real-world scenarios.

References

1. Boss, M., Braun, R., Jampani, V., Barron, J.T., Liu, C., Lensch, H.P.: Nerd: Neural reflectance decomposition from image collections. In: ICCV. pp. 12684–12694 (2021) [4](#)
2. Boss, M., Jampani, V., Braun, R., Liu, C., Barron, J., Lensch, H.P.: Neural-pil: Neural pre-integrated lighting for reflectance decomposition. In: NeurIPS. pp. 10691–10704 (2021) [4](#)
3. Charatan, D., Li, S.L., Tagliasacchi, A., Sitzmann, V.: pixelsplat: 3d gaussian splats from image pairs for scalable generalizable 3d reconstruction. In: CVPR. pp. 19457–19467 (2024) [1](#), [3](#), [9](#)
4. Chen, S., Cavallari, T., Prisacariu, V.A., Brachmann, E.: Map-relative pose regression for visual re-localization. In: CVPR. pp. 20665–20674 (2024) [6](#)
5. Chen, Y., Xu, H., Zheng, C., Zhuang, B., Pollefeys, M., Geiger, A., Cham, T.J., Cai, J.: Mvsplat: Efficient 3d gaussian splatting from sparse multi-view images. In: ECCV. pp. 370–386 (2024) [1](#), [3](#), [9](#)
6. Dosovitskiy, A., Beyer, L., Kolesnikov, A., Weissenborn, D., Zhai, X., Unterthiner, T., Dehghani, M., Minderer, M., Heigold, G., Gelly, S., Uszkoreit, J., Houlsby, N.: An image is worth 16x16 words: Transformers for image recognition at scale. In: ICLR (2021) [6](#)
7. Edstedt, J., Sun, Q., Bökman, G., Wadenbäck, M., Felsberg, M.: Roma: Robust dense feature matching. In: CVPR. pp. 19790–19800 (2024) [9](#)
8. Ha, D., Dai, A.M., Le, Q.V.: Hypernetworks. In: ICLR (2017) [7](#)
9. Hong, S., Jung, J., Shin, H., Han, J., Yang, J., Luo, C., Kim, S.: Pf3plat: Pose-free feed-forward 3d gaussian splatting. In: ICML (2025) [4](#), [9](#)
10. Hong, S., Jung, J., Shin, H., Yang, J., Kim, S., Luo, C.: Unifying correspondence pose and nerf for generalized pose-free novel view synthesis. In: CVPR. pp. 20196–20206 (2024) [9](#)
11. Huang, R., Mikolajczyk, K.: No pose at all: Self-supervised pose-free 3d gaussian splatting from sparse views. In: ICCV. pp. 27947–27957 (2025) [2](#), [3](#), [4](#), [5](#), [8](#), [9](#), [11](#), [19](#)
12. Huang, R., Mikolajczyk, K.: Spfsplatv2: Efficient self-supervised pose-free 3d gaussian splatting from sparse views (2025), arXiv preprint arXiv:2509.17246 [2](#), [3](#), [4](#), [5](#), [9](#)
13. Jensen, R., Dahl, A., Vogiatzis, G., Tola, E., Aanaes, H.: Large scale multi-view stereopsis evaluation. In: CVPR. pp. 406–413 (2014) [9](#)
14. Jiang, L., Mao, Y., Xu, L., Lu, T., Ren, K., Jin, Y., Xu, X., Yu, M., Pang, J., Zhao, F., et al.: Anysplat: Feed-forward 3d gaussian splatting from unconstrained views. TOG **44**(6), 1–16 (2025) [2](#)
15. Jiang, Y., Tu, J., Liu, Y., Gao, X., Long, X., Wang, W., Ma, Y.: Gaussianshader: 3d gaussian splatting with shading functions for reflective surfaces. In: CVPR. pp. 5322–5332 (2024) [2](#), [4](#)
16. Kang, G., Yoo, J., Park, J., Nam, S., Im, H., Shin, S., Kim, S., Park, E.: Selfsplat: Pose-free and 3d prior-free generalizable 3d gaussian splatting. In: CVPR. pp. 22012–22022 (2025) [2](#), [4](#), [9](#)
17. Kerbl, B., Kopanas, G., Leimkühler, T., Drettakis, G.: 3d gaussian splatting for real-time radiance field rendering. ACM TOG **42**(4), 1–14 (2023) [1](#), [3](#), [4](#)
18. Leroy, V., Cabon, Y., Revaud, J.: Grounding image matching in 3d with mast3r. In: ECCV. pp. 71–91 (2024) [2](#), [4](#), [5](#), [9](#)

19. Liang, R., Chen, H., Li, C., Chen, F., Panneer, S., Vijaykumar, N.: Envidr: Implicit differentiable renderer with neural environment lighting. In: ICCV. pp. 79–89 (2023) [4](#)
20. Liu, A., Tucker, R., Jampani, V., Makadia, A., Snavely, N., Kanazawa, A.: Infinite nature: Perpetual view generation of natural scenes from a single image. In: ICCV. pp. 14458–14467 (2021) [9](#), [10](#), [20](#)
21. Liu, J., Tang, X., Cheng, F., Yang, R., Li, Z., Liu, J., Huang, Y., Lin, J., Liu, S., Wu, X., et al.: Mirrorgaussian: Reflecting 3d gaussians for reconstructing mirror reflections. In: ECCV. pp. 377–393 (2024) [2](#), [4](#)
22. Liu, Y., Wang, P., Lin, C., Long, X., Wang, J., Liu, L., Komura, T., Wang, W.: Nero: Neural geometry and brdf reconstruction of reflective objects from multiview images. ACM TOG **42**(4), 1–22 (2023) [4](#)
23. Lu, T., Yu, M., Xu, L., Xiangli, Y., Wang, L., Lin, D., Dai, B.: Scaffold-gs: Structured 3d gaussians for view-adaptive rendering. In: CVPR. pp. 20654–20664 (2024) [2](#), [4](#)
24. Luiten, J., Kopanas, G., Leibe, B., Ramanan, D.: Dynamic 3d gaussians: Tracking by persistent dynamic view synthesis. In: 3DV. pp. 800–809. IEEE (2024) [5](#)
25. Mildenhall, B., Srinivasan, P.P., Tancik, M., Barron, J.T., Ramamoorthi, R., Ng, R.: Nerf: Representing scenes as neural radiance fields for view synthesis. Communications of the ACM **65**(1), 99–106 (2021) [4](#)
26. Ranftl, R., Bochkovskiy, A., Koltun, V.: Vision transformers for dense prediction. In: ICCV. pp. 12179–12188 (2021) [6](#)
27. Schonberger, J.L., Frahm, J.M.: Structure-from-motion revisited. In: CVPR. pp. 4104–4113 (2016) [2](#), [3](#)
28. Smart, B., Zheng, C., Laina, I., Prisacariu, V.A.: Splatt3r: Zero-shot gaussian splatting from uncalibrated image pairs (2024), arXiv preprint arXiv:2408.13912 [2](#), [3](#), [9](#)
29. Srinivasan, P.P., Deng, B., Zhang, X., Tancik, M., Mildenhall, B., Barron, J.T.: Nerv: Neural reflectance and visibility fields for relighting and view synthesis. In: CVPR. pp. 7495–7504 (2021) [4](#)
30. Tang, J., Chen, Z., Chen, X., Wang, T., Zeng, G., Liu, Z.: Lgm: Large multi-view gaussian model for high-resolution 3d content creation. In: ECCV. pp. 1–18 (2024) [1](#), [3](#)
31. Verbin, D., Hedman, P., Mildenhall, B., Zickler, T., Barron, J.T., Srinivasan, P.P.: Ref-nerf: Structured view-dependent appearance for neural radiance fields. In: CVPR. pp. 5481–5490 (2022) [4](#)
32. Wang, J., Chen, M., Karaev, N., Vedaldi, A., Ruppel, C., Novotny, D.: Vggg: Visual geometry grounded transformer. In: CVPR. pp. 5294–5306 (2025) [2](#), [4](#), [5](#), [9](#)
33. Wang, S., Leroy, V., Cabon, Y., Chidlovskii, B., Revaud, J.: Dust3r: Geometric 3d vision made easy. In: CVPR. pp. 20697–20709 (2024) [2](#)
34. Wang, Z., Bovik, A., Sheikh, H., Simoncelli, E.: Image quality assessment: from error visibility to structural similarity. IEEE TIP **13**(4), 600–612 (2004) [9](#)
35. Wu, G., Yi, T., Fang, J., Xie, L., Zhang, X., Wei, W., Liu, W., Tian, Q., Wang, X.: 4d gaussian splatting for real-time dynamic scene rendering. In: CVPR. pp. 20310–20320 (2024) [5](#)
36. Xu, Y., Shi, Z., Yifan, W., Chen, H., Yang, C., Peng, S., Shen, Y., Wetzstein, G.: Grm: Large gaussian reconstruction model for efficient 3d reconstruction and generation. In: ECCV. pp. 1–20 (2024) [1](#), [3](#)
37. Yang, Z., Gao, X., Sun, Y.T., Huang, Y.H., Lyu, X., Zhou, W., Jiao, S., Qi, X., Jin, X.: Spec-gaussian: Anisotropic view-dependent appearance for 3d gaussian splatting. In: NeurIPS. pp. 61192–61216 (2024) [2](#), [4](#)

38. Ye, B., Liu, S., Xu, H., Xueting, L., Pollefeys, M., Yang, M.H., Songyou, P.: No pose, no problem: Surprisingly simple 3d gaussian splats from sparse unposed images. In: ICLR (2025) [3](#), [9](#)
39. Zhang, K., Bi, S., Tan, H., Xiangli, Y., Zhao, N., Sunkavalli, K., Xu, Z.: Gs-lrm: Large reconstruction model for 3d gaussian splatting. In: ECCV. pp. 1–19 (2024) [1](#), [3](#)
40. Zhang, R., Isola, P., Efros, A.A., Shechtman, E., Wang, O.: The unreasonable effectiveness of deep features as a perceptual metric. In: CVPR. pp. 586–595 (2018) [8](#), [9](#), [19](#)
41. Zhang, X., Srinivasan, P.P., Deng, B., Debevec, P., Freeman, W.T., Barron, J.T.: Nerfactor: Neural factorization of shape and reflectance under an unknown illumination. ACM TOG **40**(6), 1–18 (2021) [4](#)
42. Zhou, T., Tucker, R., Flynn, J., Fyffe, G., Snavely, N.: Stereo magnification: Learning view synthesis using multiplane images. ACM TOG **37**(4), 1–12 (2018) [9](#), [10](#), [20](#)
43. Zhou, Y., Zhang, F., Wang, Z., Zhang, L.: Rtr-gs: 3d gaussian splatting for inverse rendering with radiance transfer and reflection. In: ACM MM. pp. 6888–6897 (2025) [2](#), [4](#)

A Additional Methodological Details

A.1 Details on Target Pose Reparameterization

In Sec. 3.3, we introduce a 4D reparameterized feature of the target pose as input to the view MLP to facilitate the prediction of view-dependent Gaussian offsets. This section details the formal mathematical derivation of the 3D unit viewing direction and the 1D log-distance from the raw target extrinsic matrix $P^{t \rightarrow 1} \in \mathbb{R}^{4 \times 4}$, following the formulation described in the main paper.

Computing the Camera Center in World Coordinates. The predicted target extrinsics $P^{t \rightarrow 1}$ represent the World-to-Camera (W2C) transformation. For any point X_w in the world (canonical) coordinate system, its position in the camera coordinate system X_c is defined as $X_c = R^{t \rightarrow 1}X_w + t^{t \rightarrow 1}$, where $R^{t \rightarrow 1} \in \mathbb{R}^{3 \times 3}$ is the orthogonal rotation matrix and $t^{t \rightarrow 1} \in \mathbb{R}^3$ is the translation vector. Since the camera center C corresponds to the origin $(0, 0, 0)^T$ in the camera coordinate system, we derive its world-coordinate position $C^{t \rightarrow 1}$ as follows:

$$0 = R^{t \rightarrow 1}C^{t \rightarrow 1} + t^{t \rightarrow 1} \implies C^{t \rightarrow 1} = -(R^{t \rightarrow 1})^T t^{t \rightarrow 1}. \quad (\text{S1})$$

Construction of the 4D Target Pose Feature. For each canonical Gaussian with center position $\mu_j^{v \rightarrow 1} \in \mathbb{R}^3$ originating from pixel j of context view v , we compute the relative pixel-wise displacement vector from the Gaussian center to the target camera center as $\mathbf{d}_j^v = C^{t \rightarrow 1} - \mu_j^{v \rightarrow 1}$. The view MLP then receives a 4D input $[\mathbf{u}_j^v, l_j^v]$, which consists of a unit viewing direction $\mathbf{u}_j^v \in \mathbb{R}^3$ and a log-scale distance $l_j^v \in \mathbb{R}$, derived from the displacement vector as follows:

$$\mathbf{u}_j^v = \frac{\mathbf{d}_j^v}{\|\mathbf{d}_j^v\|_2}, \quad l_j^v = \log(\|\mathbf{d}_j^v\|_2 + \epsilon), \quad (\text{S2})$$

where ϵ is a small constant (e.g., 10^{-6}) for numerical stability.

Rationale for Log-Scale Transformation. The choice of a log-scale for the distance parameter l is motivated by the non-linear sensitivity inherent in perspective projection. In 3D-to-2D mapping, the visual impact of camera movement is more pronounced for objects at closer ranges. By applying the $\log(\cdot)$ transformation, we compress the dynamic range of distances and maintain higher sensitivity to near-field variations. This allows the view MLP to prioritize parameter refinements for Gaussians where viewpoint changes result in the most significant visual impact, thereby improving the modeling of view-dependent appearance variations.

A.2 Detailed Formulations of Loss Functions

Image Rendering Loss. The rendering loss \mathcal{L}_{render} supervises the quality of novel view synthesis by comparing the ground-truth target image I^t with the

rendered output \hat{I}^t . As described in the main paper, this objective is defined as a weighted combination of the MSE photometric loss and the LPIPS [40] perceptual loss:

$$\mathcal{L}_{render} = \mathcal{L}_{MSE}(I^t, \hat{I}^t) + \lambda_{LPIPS} \mathcal{L}_{LPIPS}(I^t, \hat{I}^t), \quad (\text{S3})$$

where λ_{LPIPS} acts as a balancing weight. This formulation encourages the model to achieve both pixel-level photometric accuracy and feature-level perceptual similarity, leading to high-quality rendering results.

Reprojection Loss. Since our framework learns 3D Gaussian centers in a canonical space without ground-truth poses, relying solely on the rendering loss can lead to training instability and overfitting to the canonical coordinate frame. To mitigate this and ensure geometric consistency in the absence of ground-truth poses, we utilize \mathcal{L}_{reproj} , which provides explicit supervision for both the 3D Gaussian positions and the estimated camera parameters. This loss measures the alignment between the canonical 3D representations and their corresponding 2D observations.

Specifically, for each pixel p_j^v in context view v , we project the 3D Gaussian center $\mu_j^{v \rightarrow 1}$ from the canonical space to view v using the estimated relative pose $P^{v \rightarrow 1}$ and the camera intrinsics K^v . The reprojection loss is computed as:

$$\mathcal{L}_{reproj} = \sum_{v=1}^N \sum_{j=1}^{H \times W} \|p_j^v - \pi(K^v, P^{v \rightarrow 1}, \mu_j^{v \rightarrow 1})\|, \quad (\text{S4})$$

where $P^{v \rightarrow 1} \in \{P_c^{v \rightarrow 1}, P_{c+t}^{v \rightarrow 1}\}$ and $\pi(\cdot)$ denotes the camera projection function. To maintain consistency, we apply this reprojection loss to the poses estimated from both the context-only branch and the context-with-target branch. This loss stabilizes pose estimation and prevents degenerate solutions where the canonical geometry collapses.

Total Loss. The total training objective is the weighted sum of the above terms:

$$\mathcal{L}_{total} = \mathcal{L}_{render} + \lambda_{reproj} \mathcal{L}_{reproj}, \quad (\text{S5})$$

where λ_{reproj} is a weighting factor. This combined objective enables stable training of the pixel-aligned 3D Gaussians and view-dependent rendering without requiring ground-truth poses. In our experiments, we set the hyperparameters to $\lambda_{LPIPS} = 0.05$ and $\lambda_{reproj} = 0.001$.

B Additional Ablation Studies

In this section, we provide further ablation studies to validate the design choices of our **ViewSplat** framework. All experiments in this section are conducted by integrating ViewSplat framework into the SPFSplat [11] baseline.

Ablation on Target Pose Parameterization. To empirically validate the effectiveness of our proposed log-scale distance described in Eq. (S2), we conduct an ablation study comparing it against a standard linear distance metric $\|d\|_2$. As summarized in Tab. S1, the log-scale distance consistently outperforms the linear counterpart in terms of PSNR across both the RE10K [42] and ACID [20] datasets.

The improvement in PSNR indicates that the logarithmic transformation provides a more informative signal for the view MLP to refine Gaussian parameters. Specifically, while both metrics share the same normalized viewing direction, the log-scale distance representation exhibits increased sensitivity to near-field variations, allowing the model to better capture complex view-dependent effects that are most prominent at close ranges. These results confirm that reparameterizing distance to align with the non-linear nature of perspective projection enables more precise modeling of view-dependent effects than a naive linear distance representation.

Table S1: Effectiveness comparison of the proposed log-scale distance against a standard linear distance as input to the view MLP.

Method	RE10K			ACID		
	PSNR \uparrow	SSIM \uparrow	LPIPS \downarrow	PSNR \uparrow	SSIM \uparrow	LPIPS \downarrow
Linear Dist.	26.296	0.857	0.144	26.618	0.790	0.177
Log-scale Dist. (Ours)	26.317	0.857	0.144	26.661	0.790	0.177

Effect of View MLP Hidden Dimension. As shown in Tab. S2, reducing the hidden dimension D of the view MLP improves rendering speed and inference memory efficiency. Reducing D from 16 to 8 provides clear computational benefits, improving throughput by 32 FPS and reducing memory usage by 18.5%, while causing only a negligible drop in PSNR (-0.003). However, further reducing the dimension to $D = 4$ leads to a more noticeable degradation in reconstruction quality (-0.012 PSNR) while offering comparatively smaller additional speed improvements. Although our main experiments use $D = 16$ to prioritize rendering fidelity, we identify $D = 8$ as the optimal trade-off point, offering a balanced compromise between high-quality rendering and real-time efficiency.

Table S2: Quantitative evaluation of rendering quality and efficiency on RE10K with varying hidden dimension (D) of the view MLP in our ViewSplat framework.

D	PSNR \uparrow	SSIM \uparrow	LPIPS \downarrow	Inf. Time (s) \downarrow	FPS \uparrow	Mem. (GiB) \downarrow
16	26.317	0.857	0.144	0.057	154	0.648
8	26.314	0.857	0.144	0.057	186	0.528
4	26.302	0.857	0.144	0.056	207	0.487

C More Qualitative Results

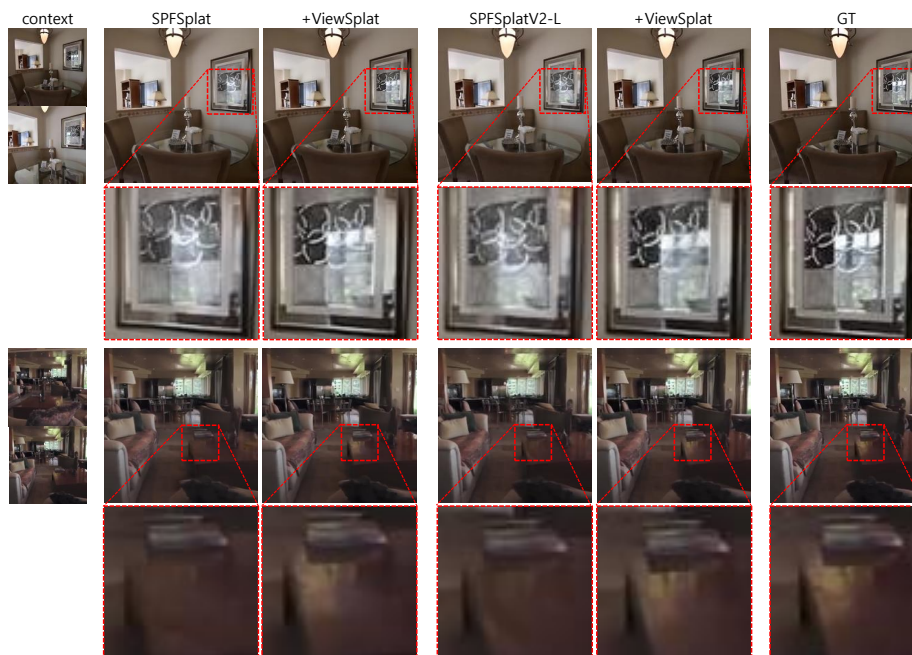


Fig. S1: More qualitative results on RE10K with large image overlap.

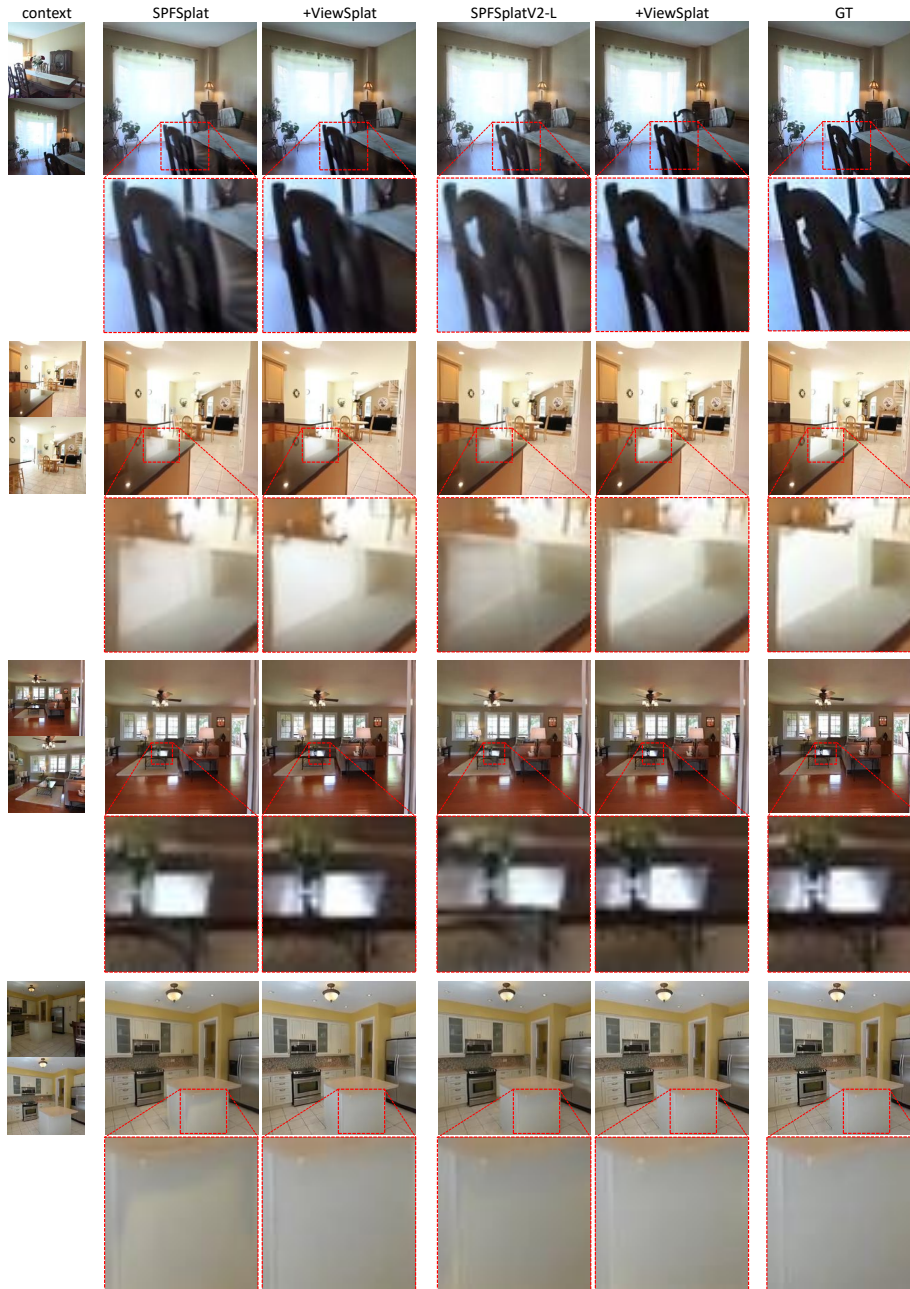


Fig. S2: More qualitative results on RE10K with medium image overlap.

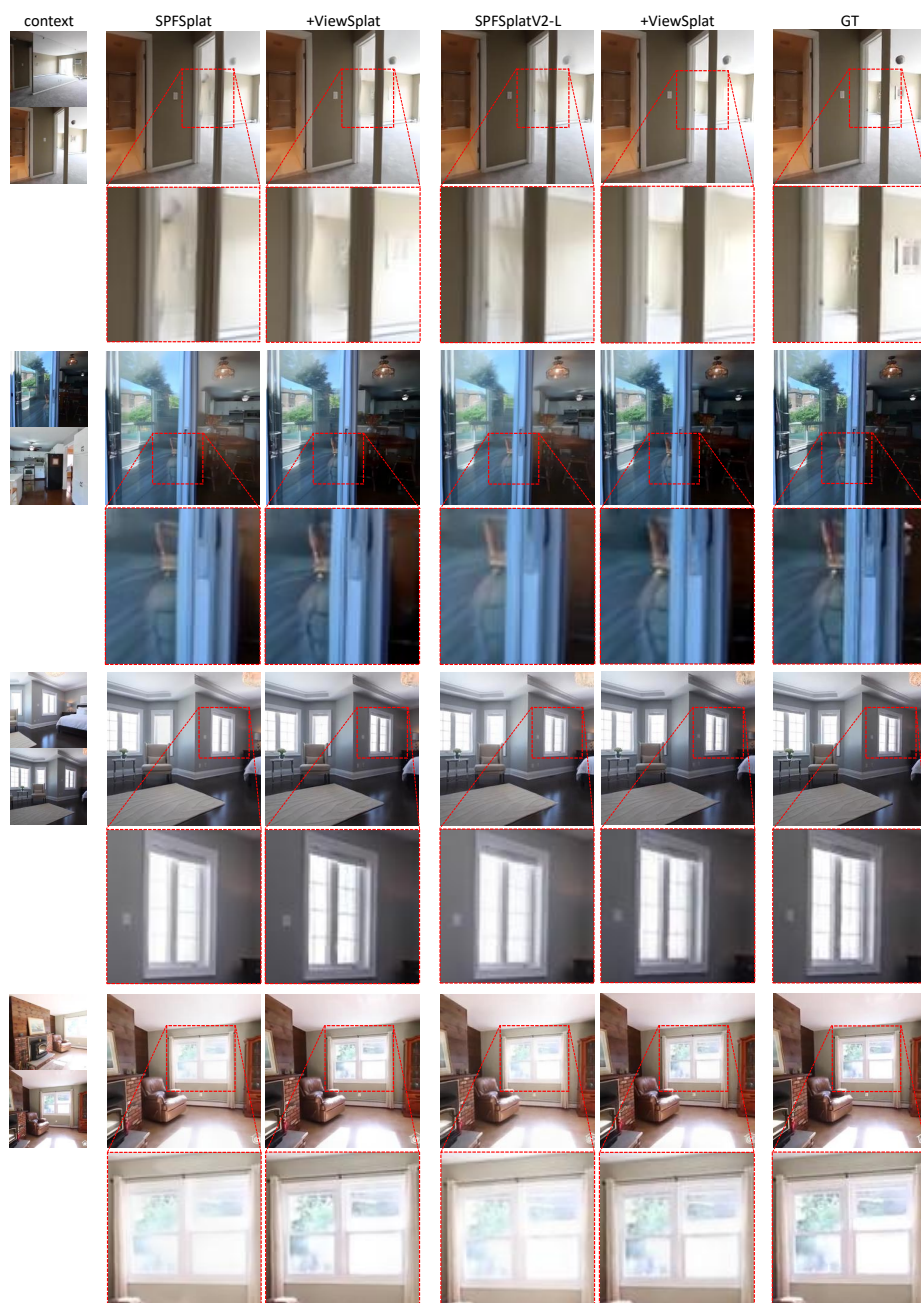


Fig. S3: More qualitative results on RE10K with medium image overlap.

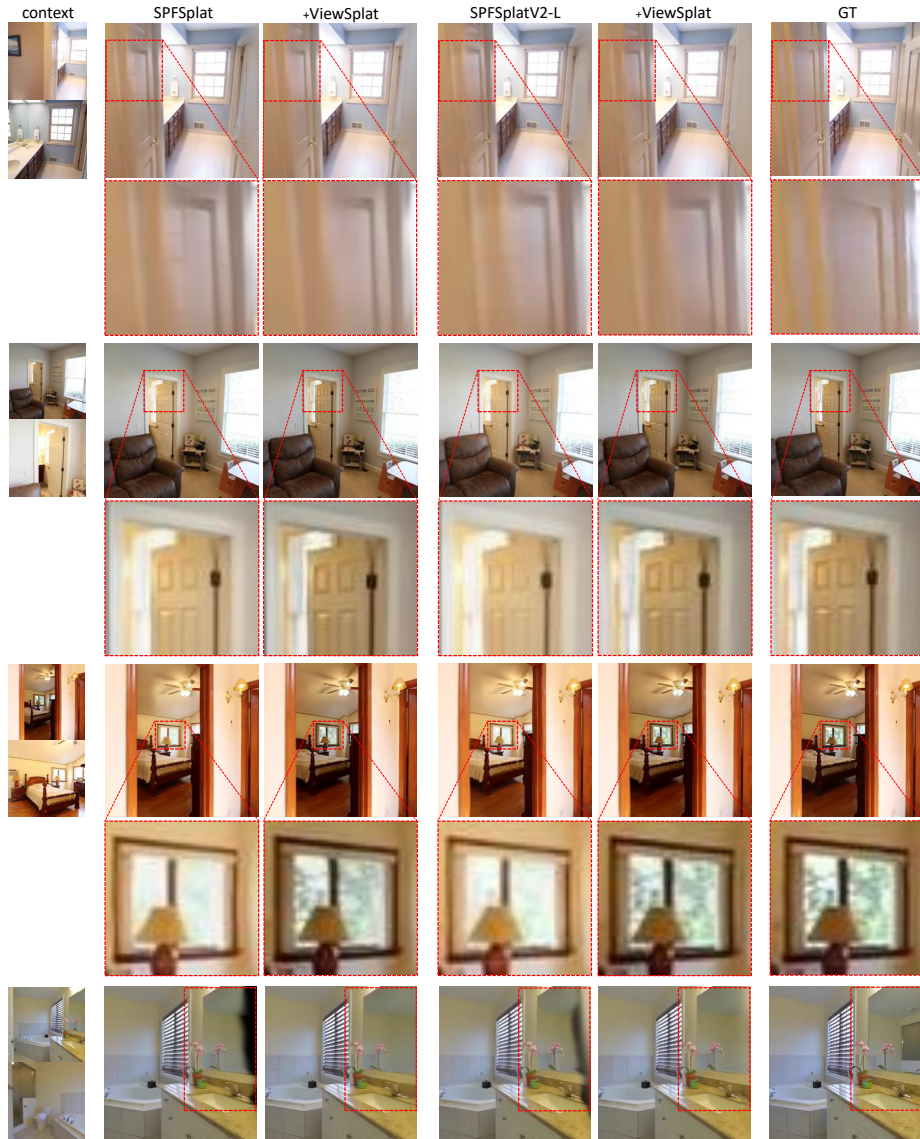


Fig. S4: More qualitative results on RE10K with small image overlap.